



One Year in the Life of Young Suns: Data-constrained Corona-wind Model of κ^1 Ceti

Vladimir S. Airapetian^{1,2}, Meng Jin³, Theresa Lüftinger⁴, Sudeshna Boro Saikia⁵, Oleg Kochukhov⁶, Manuel Güdel⁵,
Bart Van Der Holst⁷, and W. Manchester IV⁷

¹American University, 4400 Massachusetts Avenue NW, Washington, DC 20016 USA

²NASA/GSFC/SEEC, Greenbelt, MD, 20771, USA

³SETI, 189 N Bernardo Avenue 200, Mountain View, CA 94043, USA

⁴ESA, Keplerlaan 1, 2201 AZ Noordwijk, Netherlands

⁵University of Vienna, Department of Astrophysics, Türkenschanzstrasse 17, 1180 Vienna, Austria

⁶Uppsala University, Box 516, 75120 Uppsala, Sweden

⁷Atmospheric, Oceanic, and Space Sciences, University of Michigan, Ann Arbor, MI 48109, USA

Received 2021 April 25; revised 2021 June 2; accepted 2021 June 2; published 2021 August 3

Abstract

The young magnetically active solar-like stars are efficient generators of ionizing radiation in the form of X-ray and extreme-UV (EUV) flux, stellar wind, and eruptive events. These outputs are the critical factors affecting atmospheric escape and chemistry of (exo)planets around active stars. While X-ray fluxes and surface magnetic fields can be derived from observations, the EUV emission, and wind mass fluxes, coronal mass ejections and associated stellar energetic particle events cannot be directly observed. Here, we present the results of a three-dimensional magnetohydrodynamic (MHD) model with inputs constrained by spectropolarimetric data, Hubble Space Telescope/STIS far-UV and X-ray data, and stellar magnetic maps reconstructed at two epochs separated by 11 months. The simulations show that over the course of the year the global stellar corona had undergone a drastic transition from a simple dipole-like to a tilted dipole with multipole field components and thus provided favorable conditions for corotating interaction regions (CIRs) that drive strong shocks. The dynamic pressures exerted by CIRs are 1300 times larger than those observed from the Sun and can contribute to the atmospheric erosion of early Venus, Earth, Mars, and young Earth-like exoplanets. Our data-constrained MHD model provides the framework to model coronal environments of G–M planet-hosting dwarfs. The model outputs can serve as a realistic input for exoplanetary atmospheric models to evaluate the impact of stellar coronal emission, stellar winds, and CIRs on their atmospheric escape and chemistry that can be tested in the upcoming James Webb Space Telescope and ground-based observations.

Unified Astronomy Thesaurus concepts: G dwarf stars (556); Stellar coronae (305); Stellar winds (1636); Planet hosting stars (1242); Exoplanets (498); Magnetohydrodynamics (1964)

1. Introduction

The “Sun-In-Time” and recent multiwavelength observations performed with Kepler, TESS, XMM-Newton, and ground-based observations suggest that young (the first 0.5 Gyr) solar analogs (G-type main-sequence stars) are magnetically active stars (Güdel 2007, 2020; Airapetian et al. 2020). Their magnetic activity is manifested in the form of large starspots covering up to 10% of a stellar surface, strong surface magnetic fields up to a few hundred gauss, dense and hot X-ray-bright coronae, massive fast winds, and frequent flare activity (Güdel 2007; Sanz-Forcada et al. 2011; Maehara et al. 2012; Notsu et al. 2019; Sanz-Forcada et al. 2019; Airapetian et al. 2020; Kochukhov et al. 2020). The characterization of coronal activity and its output, stellar winds, will help in understanding the evolution of angular momentum of stars with age as fast and massive stellar winds carry away significant angular momentum of cool stars, and thus contribute to magnetic braking, which in turn controls stellar magnetic dynamo and its activity (Brun & Browning 2017; Gallet et al. 2017; O’Fionnagain et al. 2019; Vidotto 2021).

Recent studies recognized the critical impact of stellar magnetic activity on atmospheric evolution of exoplanetary environments as a factor of their habitability (see Cohen et al. 2014, 2018; Airapetian et al. 2016; Cuntz & Guinan 2016; Airapetian et al. 2017; Dong et al. 2018; Yamashiki et al. 2019; Airapetian et al. 2020 and references therein). The accurate

knowledge of stellar XUV (X-ray (0.1–10 nm) and extreme-UV fluxes (EUV, 10–91.2 nm)) and stellar wind fluxes are critical inputs for the atmospheric escape and chemistry models (Cohen et al. 2014; Cuntz & Guinan 2016; Airapetian et al. 2017; Garcia-Sage et al. 2017; Johnstone et al. 2019; Johnstone 2020; Airapetian et al. 2020). XUV radiation deposits heating via photoionization of exoplanetary atmospheres that increases neutral temperature with overall expansion transitioning at some point to hydrodynamic escape from the planetary atmospheres. These ionizing fluxes can also erode planetary atmospheres via production of photoelectrons that drive polarization electric field, the source of ion outflow. Both effects can be instrumental in driving massive winds from terrestrial-type exoplanets and therefore negatively impact exoplanetary habitability. Massive and magnetized stellar winds from young stars can exert dynamic pressure on exoplanetary magnetospheres, thus leading to the expansion of the polar cap area, as well as generate ionospheric currents that can dissipate their energy via Joule heating, which is another factor of atmospheric escape via thermal plasma expansion (Cohen et al. 2014, 2018). Thus, accurate knowledge of the EUV and wind fluxes are critical factors in assessing the atmospheric escape rates and thus atmospheric evolution of Venus, Earth, Mars, and exoplanets. Also, stellar winds carry away significant angular momentum of young cool stars and thus control evolution of the stellar rotation rate,

which in turn governs stellar magnetic activity (Weber & Davis 1967; Sakurai 1985; Kawaler 1988).

While the X-ray portion and short-wavelength portion of EUV flux (up to 30 nm) can be derived from direct soft X-ray observations, emission measure distribution, and, in a few cases of very close stars, direct EUV observations (e.g., EUVE mission), the total EUV flux longer than 30 nm is heavily absorbed by neutral hydrogen of the interstellar medium (ISM) and thus cannot be reliably determined (Ribas et al. 2005; Sanz-Forcada et al. 2011; Duvvuri et al. 2021).

Also, tenuous stellar winds cannot be directly observed and characterized but can be empirically constrained using astrophysical Ly α measurements, radio observations, and other proxies (Wood et al. 2005; Fichtinger et al. 2017; Jardine & Collier-Cameron 2019). Wood et al. (2005) found that the mass-loss rates of winds can be scaled with the X-ray coronal flux of many magnetically active solar-like stars, which suggests that the stellar coronal heating and stellar wind acceleration are physically connected phenomena (Airapetian & Cuntz 2015; Cranmer et al. 2015).

On the Sun, the origin of supersonic and magnetized wind is physically linked to the presence of hot, 1–5–2 MK solar coronal plasma. If the slow component (450 km s⁻¹) of the solar wind can be understood as driven by the thermal pressure gradient of the hot 1.5–2 MK solar corona by a simple steady-state Parker’s model (1958), the acceleration of the fast wind (750 km s⁻¹) that emanated from coronal holes was left unspecified. This question was later discussed in a number of studies that suggested an additional momentum term via Alfvén waves to address this problem (Usmanov et al. 2000; Ofman 2010; Airapetian & Cuntz 2015; Cranmer et al. 2015). Thus, theoretical modeling of stellar coronae that predicts X-ray coronal flux can be used as one of the methods to characterize the properties of stellar winds.

While it is generally understood that the magnetic field is the ultimate source of energy for coronal heating and wind acceleration, the details of how magnetic energy is transferred from the solar photosphere into the corona remain unsolved. Two major mechanisms have been invoked to explain the coronal heating as traced by EUV lines. The first mechanism assumes that quasi-static small-scale (granular) photospheric motions tangle, twist, and braid the magnetic field, building up magnetic free energy, which is then converted into heat via miriads of magnetic reconnection events referred to as nanoflares (e.g., Parker 1972, 1988; Klimchuk 2006; Dahlburg et al. 2016). The second heating mechanism involves the generation and propagation of magnetohydrodynamic (MHD) waves, the Alfvén or magnetosonic waves driven by photospheric motions depositing their energy into the chromosphere, transition region, and corona via resonant absorption, phase mixing, or turbulent dissipation (Osterbrock 1961; Banerjee et al. 2009; Hahn & Savin 2013; Mathioudakis et al. 2013; Cranmer & Winebarger 2019). Recent solar observations provide evidence for energy transport via upward-propagating large-amplitude Alfvén waves in the solar chromosphere, transition region, and corona (De Pontieu et al. 2007; Tomczyk et al. 2007; Jess et al. 2009; McIntosh et al. 2011; Mathioudakis et al. 2013). The wave amplitudes are inferred from the Doppler line-of-sight (LOS) velocity perturbation and nonthermal broadening of optically thin emission lines. Recently, Grant et al. (2018) presented evidence of Alfvén wave dissipation at small scales as expected from the MHD

wave theory using the results of high spatial resolution observations of the chromospheric layers associated with the umbral boundary of a sunspot.

Large nonthermal broadening of emission lines forming in the upper atmosphere has also been detected in a number of active cool main-sequence stars, as well as giant and supergiant stars (Wood et al. 1997; Peter 2006; review in Airapetian & Cuntz 2015). In most cases, the nonthermally broadened emission lines show enhanced wings, so that the line profile can be fit by two Gaussian profiles. While these features may also be interpreted as a signature of microflaring activity as suggested by Wood et al. (1997), they have been observed in late-type (K and M) giant stars that show no signatures of eruptive activity. Carpenter (1995) and Airapetian et al. (2000) suggested that broad and enhanced wings of optically thin emission lines can be represented by large-scale supersonic turbulent motions, which are anisotropically distributed either along or perpendicular to the LOS. Supersonic turbulent motions can be attributed to unresolved motions associated with upward- and/or downward-propagating large-amplitude (nonlinear) Alfvén waves that can efficiently dissipate in the solar and stellar upper atmosphere via shocks (Airapetian et al. 2000; Suzuki & Inutsuka 2006; Airapetian et al. 2010; Airapetian and Cuntz 2015; Magyar and Nakariakov 2020; Shoda et al. 2021). These signatures can also be formed via interaction of upward- with downward-propagating Alfvén waves forming as a result of reflection from the atmospheric regions, where the gradient of the Alfvén velocity is comparable to or exceeds the Alfvén wave frequency, or in coronal loops (Verdini & Velli 2008; Cranmer & Winebarger 2019 and references herein). Moreover, recent Parker Solar Probe observations of the solar wind at 36 R_{\odot} suggest highly dynamic environments driven by a spectrum of Alfvénic fluctuations and “are not indicative of impulsive processes in the chromosphere or corona” (Chen et al. 2020; Squire et al. 2020).

To model X-ray emission of the corona of the Sun and solar-type stars, researchers applied two classes of three-dimensional (3D) MHD numerical models. The first class of models assumes ad hoc, thermally driven, nearly isothermal coronae and solar and stellar winds (Cohen et al. 2008; van der Holst et al. 2014; Vidotto et al. 2015; Alvarado-Gómez et al. 2016a, 2016b; Do Nascimento et al. 2016; Lynch et al. 2019). However, these polytropic models cannot quantitatively address data from the solar EUV and X-ray emission and thus require a more accurate equation for the energy transport. The second class of MHD coronal and wind models solves the full energy equation (so-called thermodynamic MHD) that specifies the heating and cooling terms of the solar atmosphere and the wind. Here, the heating terms are either specified as the ad hoc heating term that varies with height or due to the dissipation of turbulent cascade introduced by Alfvén waves, while cooling terms include thermal conduction and radiative cooling via optically thin emission lines (Usmanov et al. 2000, 2018; Lionello et al. 2009; van der Holst et al. 2014; Alvarado-Gómez et al. 2016a, 2016b; Airapetian & Usmanov 2016; Oran et al. 2017; Boro Saikia et al. 2020). An advantage of a 3D MHD code, AWSoM, is in modeling the solar coronal X-ray and EUV fluxes by extending the lower boundary from the inner corona to the upper chromosphere, where the Poynting flux of Alfvén waves can be constrained directly from the spectroscopic observations. This model thus can be constrained

by the data supplied from the solar chromospheric emission lines (Oran et al. 2013, 2017). The model assumes that the solar corona is heated predominantly by the dissipation of Alfvén waves and can successfully reproduce the overall global structure of the solar corona, the X-ray and EUV emission from active regions, and the solar wind temperature, density, and magnetic field (van der Holst et al. 2014; Oran et al. 2017).

Inspired by these applications to the Sun, the AWSoM code was applied for stellar coronal and wind environments of cool stars by Alvarado-Gómez et al. (2016a, 2016b). All these studies utilized observationally derived ZDI magnetograms as model input, but the Alfvén wave flux was not constrained by observations of the simulated stars. Boro Saikia et al. (2020) also used this model to study the effect of low-resolution stellar magnetograms to simulate the wind mass-loss rates from the Sun and a young solar-like star, HN Peg. The results suggest that the solar wind model based on synoptic magnetograms derived from solar Global Oscillation Network Group (GONG) magnetograms degraded to the low spherical harmonic number ($l_{\max} = 5-10$) do not significantly affect the solar wind mass-loss rates as compared to the high-resolution magnetograms, because the wind structure is not sensitive to small-scale magnetic field structures. However, the stellar coronal X-ray and EUV emission was not addressed in these studies.

Here, we present the results of data-constrained fully thermodynamic data-constrained 3D MHD models of the solar corona and the wind at the rising phase of Solar Cycle 24 and the stellar corona of a young (~ 650 Myr) solar analog, κ^1 Ceti (HD 20630). The paper is organized as follows. Section 2 describes the data-driven AWSoM models for the Sun and κ^1 Ceti. In Section 3, we present the results of MHD simulations of the global corona of κ^1 Ceti at two different epochs and describe the stellar wind and corotating interaction regions (CIRs) from κ^1 Ceti. In Section 4, we discuss the implications of this modeling methodology for various active stars and the impact on the early Earth and terrestrial-type exoplanets around active stars.

2. Data-driven 3D MHD Corona and Wind Model

To model the solar and stellar corona-wind system of κ^1 Ceti, we used a data-constrained Alfvén-wave-driven 3D MHD numerical model, AWSoM. This is a first-principles global model that describes the stellar atmosphere from the top of the chromosphere and extends it into the heliosphere beyond Earth’s orbit. The AWSoM model is a part of the Space Weather Modeling Framework (SWMF) developed at the University of Michigan. This framework provides a high-performance computational capability to simulate solar activity induced by the magnetic flux from the upper chromosphere to the solar wind and planetary environments (Tóth et al. 2005; Jin et al. 2012, 2017; van der Holst et al. 2014; Oran et al. 2017).

The AWSoM model solves a set of two-temperature (electrons and protons) MHD equations for fully ionized plasma in the heliographic rotating frame by the shock-capturing MHD BATS-R-US code (Tóth et al. 2005). The model assumes that the Hall effect is negligible and the electrons and protons have the same bulk velocity. Thus, the code uses single-fluid continuity and momentum equations with separate pressure equations for electrons and protons. The AWSoM consists of two modules describing solar/stellar corona (SC) and inner helio/astrosphere (IH), respectively. The

SC module uses a 3D spherical grid with the radial coordinate ranging from 1 to $24 R_{\odot}$. The grid is highly stretched toward the star with smallest radial cell size $\Delta r = 10^{-3} R_{\odot}$ to numerically resolve the steep density gradients in the upper chromosphere and transition region. The IH module describes the helio/astrosphere from 16 to $250 R_{\odot}$, so that SC and IH overlap. Thus, to obtain the solution from the Sun to Earth, we couple the SC and IH components.

The MHD equations are coupled to wave kinetic equations for propagating parallel and antiparallel Alfvén waves (van der Holst et al. 2014). A steady-state solar wind solution is obtained with the local time stepping and second-order shock-capturing scheme. In this model, the low-frequency (compared to the ion cyclotron frequency) torsional Alfvén waves launched at the upper chromosphere (lower computational boundary) drive the plasma dynamics by exchanging momentum and energy with the plasma: gradients in the wave pressure accelerate the plasma, while dissipation converts wave energy into thermal energy. The model includes two equations that describe the amplitudes of propagating low-frequency Alfvén waves parallel and antiparallel to the magnetic field and are coupled to the MHD equations.

Alfvén wave energy dissipation is the only explicit source of coronal heating incorporated into the energy equation, and no ad hoc or geometric heating functions are used in this model. This global coronal model does not resolve the wave motions, because the timescales and spatial scales associated with the wave processes are much smaller than the characteristic scales of the corona. This allows us to treat the wave energy evolution under the WKB approximation. In our model, the coronal heating is driven by the magnetic energy propagated and dissipated via turbulent cascade of Alfvén waves in both closed- and open-field regions. As low-frequency Alfvén waves propagate upward into a gravitationally stratified stellar atmosphere, they become subject to reflection from regions of high gradients of Alfvén velocity (Heinemann & Olbert 1980; An et al. 1990). The interaction of downward-reflected Alfvén waves with upward-propagated ones can ignite a turbulent cascade of Alfvén waves in the lower solar atmosphere and provide a dominant source for heating the solar and stellar coronae and winds in open-field regions (Cranmer & Saar 2011; Sokolov et al. 2013). Within the closed loop-like magnetic structures the waves of different polarities (along and opposite to the direction of the loop magnetic field) can interact in a similar fashion, producing the heating within the coronal active regions. The AWSoM model provides the self-consistent evolution of the wave energy coupled to an MHD plasma of the solar corona (see van der Holst et al. 2014 for details). The wave energy in this model represents the time average of the perturbations due to a turbulent spectrum of Alfvén waves. Because energy dissipation of these waves controls the density and the temperature of the stellar corona, the accurate knowledge of the Poynting flux needs to be constrained from spectroscopic observations of stellar chromospheres. The plasma density and the Alfvén wave amplitude can be derived from the far-UV optically thin spectral lines forming at about 50,000 K specified by the AWSoM model. To model the solar corona, studies use Interface Region Imaging Spectrograph (IRIS) high spectral observations of fully resolved profiles of O IV and Si IV emission lines (Oran et al. 2017). The model inputs include high spatial resolution solar magnetograms and Alfvén wave energy flux specified at the inner boundary, the upper chromosphere at 50,000 K as the

Table 1
Observational Properties of the Current and the Young Sun Represented by κ^1 Ceti

Star ID	Sp Type	T_{eff} (K)	Mass	Log (g)	P_{rot} (days)	i (deg)	Age (Myr)	Log (L_x)
κ^1 Ceti	G5V	5705	1.02	4.49	9.2	60	650	28.79
Sun	G5V	5780	1	4.5	27	0	4650	27

wave Poynting flux normalized to the magnetic field, S_A/B . This parameter can be derived directly from NASA’s IRIS of fully resolved spectral emission lines of O IV and Si IV ions forming in the upper atmosphere (Sokolov et al. 2013; Young et al. 2018). In stellar wind models S_A/B input Alfvén wave energy flux is not directly constrained from observations, but is scaled with the stellar X-ray flux and the surface magnetic flux (Pevtsov et al. 2003; Garraffo et al. 2016; Dong et al. 2018). However, this requires prior information of the star’s X-ray activity. As stellar X-ray activity is known to exhibit variations, this approach will also lead to variations in SA/B for a magnetically variable star. In the solar case the Alfvén wave Poynting flux is well constrained from observations and nearly constant for all solar simulations. The value of S_A/B is a critical input parameter, and the wind mass flux is roughly proportional to the solar/stellar wave Poynting flux (Cranmer & Saar 2011; Boro Saikia et al. 2020).

3. Simulation Results

To model the global solar and stellar corona-wind system of κ^1 Ceti, we used a data-constrained Alfvén-wave-driven, global MHD numerical model, AWSoM. The global parameters for these two stars are presented in Table 1. In Section 3.1, we present the model inputs and steady-state solutions for the solar coronal structure and the solar wind simulated for Carrington Rotation (CR) 2106, which is representative of the early rising phase of Solar Cycle 24. For both models, we calculated thermodynamic parameters such as temperature, density, magnetic field, and velocity of global solar corona. These parameters are used to build synthetic coronal emission maps in soft X-ray band (0.25–4 keV) and EUV lines, including at 284 and 335 Å and the soft X-ray 1–8 Å band (referred to as SXR), to derive the benchmark solar model for the stellar coronal model of κ^1 Ceti. In Section 3.2, we present the results of the 3D MHD modeling of the corona of κ^1 Ceti in SXR and EUV bands and discuss the structures of the associated stellar wind at two epochs, 2012.8 and 2013.7.

3.1. Global Coronal Model of the Sun: Carrington Rotation 2106

To compare the current Sun’s coronal and wind fluxes with the corresponding fluxes from κ^1 Ceti, we performed the model of global solar corona with AWSoM at the phase near solar minimum for CR 2106. This corresponds to the rising phase of Solar Cycle 24. The inner boundary condition of the solar surface magnetic field is specified by a global magnetic map sampled from an evolving photospheric flux transport model for the period of 2011 January 20–February 11 (Schrijver & De Rosa 2003). The input Alfvén wave Poynting flux normalized to the magnetic field is specified at the lower boundary of the Sun, the upper chromosphere, and described as

$$P_w = \frac{S_A}{B_0} = \sqrt{\frac{\rho}{4\pi}} \langle \delta V^2 \rangle. \quad (1)$$

The solar coronal model uses the input plasma density of $2 \times 10^{11} \text{ cm}^{-3}$ at 50,000 K and the Alfvén wave amplitude $(\langle \delta V^2 \rangle)^{1/2} = 15 \text{ km s}^{-1}$ derived from O IV and Si IV spectral lines derived from IRIS data (see discussion in Sokolov et al. 2013; van der Holst et al. 2014, Oran et al. 2017). These parameters output the Poynting flux, $P_{w0} = (S_A/B_0)_\odot = 1.1 \times 10^5 \text{ erg cm}^{-2} \text{ G}^{-1}$. We will use this reference-normalized solar chromospheric Alfvén wave Poynting flux for our stellar coronal model discussed in Section 3.2. The adjustable input parameters include the transverse correlation length at the inner boundary, L_\perp , and the pseudo-reflection coefficient, C_{refl} , as discussed in detail by Oran et al. (2013).

We have performed the 3D MHD simulations of the solar corona until the solution is converged to steady-state coronae and the wind solution. We then used the 3D model density and temperature simulated values to synthesize coronal emission maps at Fe XV 284 Å and Fe XVI 335 Å EUV emission lines and GOES 1–8 Å soft X-ray flux by integrating along the LOS toward the observer using the CHIANTI 7.1 atomic database for solar abundances (Dere et al. 1997). The total intensity integrated over the solar disk at 1 au in the soft X-ray 1–8 Å band is $2.7 \times 10^{-5} \text{ erg cm}^{-2} \text{ s}^{-1}$, while the intensities in EUV lines, Fe XV 284 Å and Fe XVI 335 Å coronal lines, are 0.014 and $0.005 \text{ erg cm}^{-2} \text{ s}^{-1}$, respectively. These fluxes and GOES (1–8 Å) band fluxes appear to be consistent with observed values in the rising phase of SC 24 (see, e.g., Winter & Balasubramaniam 2014; Huang et al. 2016). The simulated mass-loss rate of the Sun during CR 2106 is $1.8 \times 10^{12} \text{ g s}^{-1}$ (or $2.86 \times 10^{-14} M_\odot \text{ yr}^{-1}$), and the minimum and maximum dynamic pressures of the solar wind, ρV_w^2 , over Earth’s orbit are 0.7 and 6.6 nPa, respectively. These values are consistent with Wind observations of the solar wind at 1 au (Mishra et al. 2019). The MHD model outputs, including the SXR band and EUV coronal line intensities and solar wind mass-loss rate, are presented in Table 1.

3.2. Global Coronal Model of κ^1 Ceti

κ^1 Ceti is a young (750 Myr old), nearby ($9.16 \pm 0.06 \text{ pc}$) G5V dwarf. Its age of 750 Myr was estimated by Güdel et al. (1997) from the rotation rate of 9.2 days, but later age estimates suggest an earlier age of $\sim 600 \text{ Myr}$ (Ribas et al. 2010), which makes this star one of the best proxies of the young Sun at the time when life started on Earth (Cnossen et al. 2007; Ribas et al. 2010; Do Nascimento et al. 2016). κ^1 Ceti was the subject of a number of comprehensive multiwavelength studies that provided the measurements of its surface magnetic field, chromosphere, transition region and coronal fluxes, surface spot, and flare activity (Güdel et al. 1997; Schaefer et al. 2000; Messina & Guinan 2002, 2003; Ribas et al. 2005; Telleschi et al. 2005; Do Nascimento et al. 2016; Rosén et al. 2016). The star shows the signatures of magnetic activity in the form of intense X-ray coronal flux enhanced by a factor of 40 with respect to the solar flux at solar maximum, energetic flares, and the presence of large starspots covering from 1% to 9% of the

stellar hemisphere (Schaefer et al. 2000; Walter et al. 2007). To model the global stellar corona-wind system of κ^1 Ceti, we used the AWSoM model with the input stellar magnetogram derived from spectropolarimetric observations of the star at two epochs as discussed in Section 3.2.1 and Alfvén wave flux constrained from the Hubble Space Telescope (HST)/STIS observations of the star presented in Section 3.2.2.

3.2.1. Magnetic Map of κ^1 Ceti

The stellar magnetic field can be specified by a photospheric magnetic map derived from spectropolarimetric observations. The unsigned magnetic field averaged over the stellar surface, fB , can be directly derived from unpolarized (Stokes I) observations using the Zeeman broadening technique (Reiners & Basri 2006; Kochukhov et al. 2020). Global stellar photospheric magnetic field can also be reconstructed by inverting time series of high-resolution spectropolarimetric data (circularly polarized Stokes V profiles) with the procedure known as the Zeeman Doppler Imaging (ZDI) technique (Semel 1989). Here we used the surface magnetic field maps of κ^1 Ceti (see Figure 1) at two different epochs, 2012.8 and 2013.7. These maps were reconstructed by Rosén et al. (2016) from the time-series Stokes V observations with the spectropolarimeter NARVAL at the 2 m Telescope Bernard Lyot at the Pic du Midi Observatory (France) and the spectropolarimeter HARSPol at the ESO 3.6 m telescope in La Silla, Chile.

The ZDI analysis proceeded as follows. First, the signal from a large set of spectral lines was combined in order to obtain a set of high signal-to-noise ratio mean line profiles, which is necessary for detecting weak polarization signatures. This multiline analysis was accomplished by applying the least-squares deconvolution technique (LSD; Donati et al. 1997; Kochukhov et al. 2010) using a line list retrieved from the VALD3 database for a MARCS stellar atmosphere (Gustafsson et al. 2008) with $T_{\text{eff}} = 5750$ K and $\log g = 4.4$. Only lines stronger than 20% of the continuum were used, and spectral regions contaminated with tellurics or dominated by particularly strong and broad spectral lines were removed. The LSD Stokes IV profiles were then computed with the LSD code described by Kochukhov et al. (2010). The resulting circular polarization profiles for 2012 September (2012.8) and 2013 August (2013.7) epochs of observations of κ^1 Ceti are shown in the left panel of Figure 1.

To reconstruct the large-scale photospheric magnetic field geometry of κ^1 Ceti, Rosén et al. (2016) used the Zeeman Doppler imaging code InversLSD (Kochukhov et al. 2014). They assumed the projected rotational velocity of 5 km s^{-1} (Valenti & Fischer 2005) and an inclination angle of 60° . The stellar magnetic field geometry was parameterized using a spherical harmonic expansion truncated at $l_{\text{max}} = 5$. The resulting maps of the radial (B_r), azimuthal (B_ϕ), and meridional (B_θ) field components are presented in the right panel of Figure 1 for the epochs of 2012.8 and 2013.7, respectively. The maximum angular degree assumed in the ZDI analysis corresponds to the large-scale field with resolved scales $> 180^\circ / l_{\text{max}}$ (Morin et al. 2010; Johnstone et al. 2014) and thus misses about 90% of the magnetic flux associated with small-scale structures, including starspots, and due to flux cancellation effects (See et al. 2019). Indeed, for κ^1 Ceti, the unsigned magnetic field varies between 450 and 550 G (Saar and Baliunas 1992; Kochukhov et al. 2020) and is a factor of

~ 20 greater than the global field derived from these ZDI magnetograms, which is also consistent with simulations for active solar-type stars (Lehmann et al. 2019). Thus, this model can only account for the magnetic flux from the large-scale structures; this represents the low bound of the surface magnetic flux of this star.

The surface magnetic field was then extrapolated to a 3D potential field source surface (PFSS; Wang & Sheeley 1992) solution using the finite-difference iterative potential-field solver (FDIPS). The PFSS model assumes the potential (current-free) magnetic field ($\nabla \times \mathbf{B} = 0$) that satisfies Laplace’s equation ($\nabla^2 \Phi = 0$). As an upper boundary condition, we assume that the magnetic field becomes radial at a *source surface*, which is taken to be at a height of $2.5 R_\odot$. The FDIPS method avoids the ringing patterns near regions of concentrated magnetic fields to which the spherical harmonics method is susceptible. Figure 1 shows that magnetic field components change dramatically in geometry and magnitude over 11 months of observations. The top panel of Figure 1 suggests that the global magnetic field is mostly poloidal and resembles the global field of our Sun during solar minimum, while 11 months later it became tilted at 45° with respect to the ecliptic plane with the presence of the toroidal component to be discussed in Section 3.2.3. Such variability of global magnetic field geometry on a timescale of a few months to 1 yr is a typical signature of young solar-like stars that is traced by ZDI magnetograms of young solar-type stars like BE Ceti and HN Peg and resulting X-ray coronal emission fluxes (Güdel 2007; Boro Saikia et al. 2015; Rosén et al. 2016). It is interesting to mention that a young, 300 Myr old solar-like star, χ^1 Ori, also shows a short (a few months) variability in the large-scale magnetic field structure (Waite et al. 2017).

3.2.2. The Input Alfvén Wave Poynting Flux for κ^1 Ceti

At the lower computational boundary of the AWSoM model, we specify the Poynting flux of Alfvén waves normalized to the local magnetic field, $P_w = S_A / B_0$, as

$$P_{AW} = \sqrt{\frac{\rho}{4\pi}} \langle \delta V^2 \rangle, \quad (2)$$

where ρ is the plasma mass density and $\langle \delta V^2 \rangle$ is the square of the Alfvén wave amplitude averaged over a timescale greater than the wave period (Sokolov et al. 2013). In Equation (1), the incompressible Alfvén wave density and the velocity fluctuations vary independently in the chromosphere, as the waves are weakly nonlinear. As waves propagate upward, their amplitude increases with height, and as Alfvén waves become strongly nonlinear, they excite longitudinal waves (Sabri et al. 2020).

To obtain the normalized Poynting at the upper chromosphere of κ^1 Ceti, $(S_A / B_0)_{\text{star}}$, we derived the input chromospheric plasma density of the star from the HST/STIS far-UV observed (E140M mode) fully resolved spectral lines O IV $\lambda\lambda 1399.78, 1401$ and Si IV $\lambda\lambda 1401, 1393$ in spectra of κ^1 Ceti presented in Figure 2.

We derive the estimate on the plasma density, in the upper atmosphere from the flux ratios of the density sensitive emission lines $R1 = \text{O IV } 1399.78 / 1401.16 \text{ \AA} = 0.5$ and $R3 = \text{Si IV } 1404.85 \text{ \AA} / \text{Si IV } 1406.06 \text{ \AA} = 0.51$ as discussed by Polito et al. (2016) and Young et al. (2018). These two emission line ratios provide the lower limit for the plasma

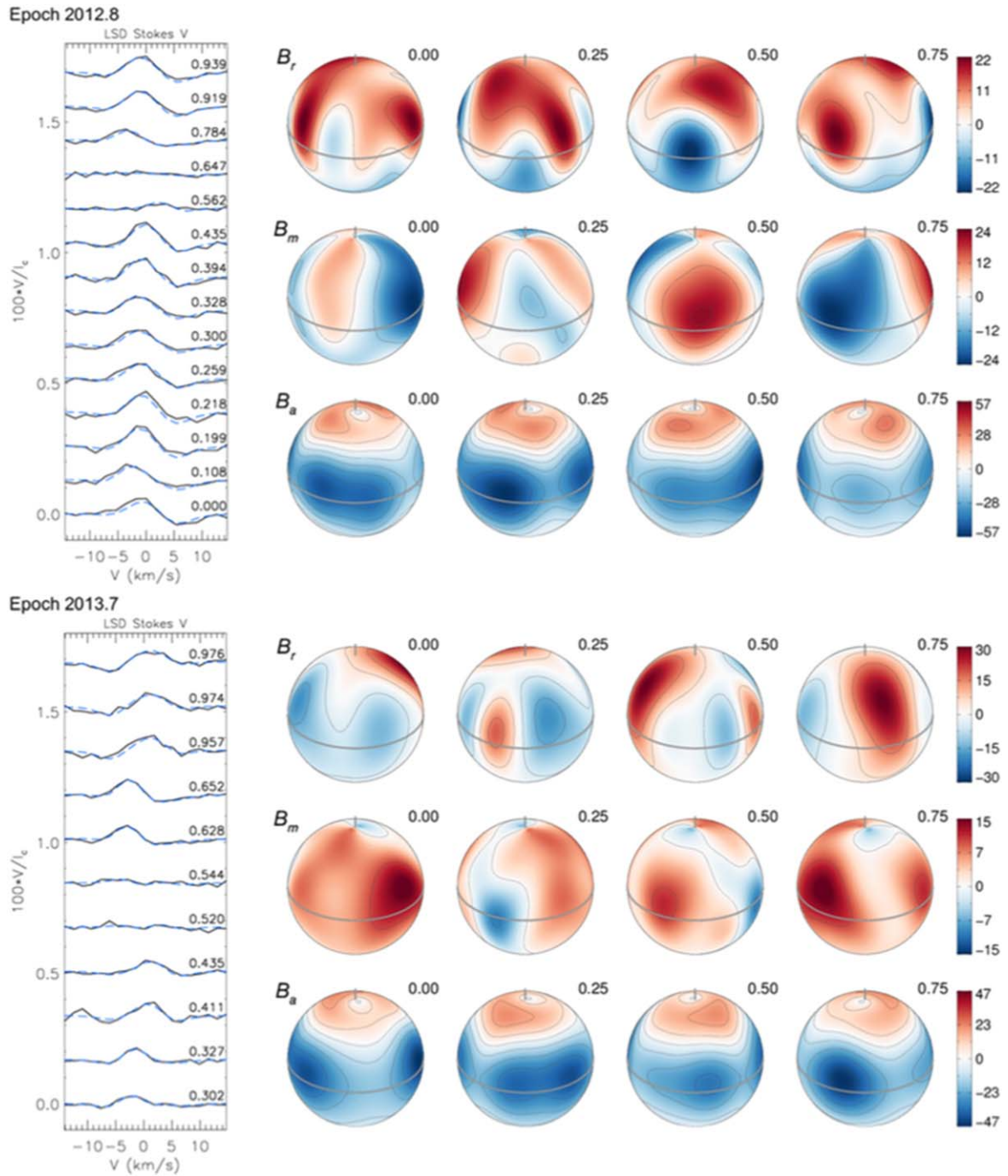


Figure 1. LSD Stokes V profiles (left panel) and the reconstructed global radial (B_r), azimuthal (B_ϕ), and meridional (B_θ) field components (right panel) of κ^1 Ceti for the epochs of 2012.8 and 2013.7, respectively, shown for four rotation phases (Rosén et al. 2016).

density of $= 1.67 \times 10^{-12} \text{ g cm}^{-3}$. It is interesting to note that the derived density of the stellar chromosphere in a quiescent state is consistent with the density inferred from R1 and R3 lines during M-class solar flare. Here, in order to study the sensitivity of the output coronal emission and stellar wind fluxes to the input density, we will consider two models with the Poynting flux input plasma density of 10^{13} cm^{-3} . The amplitude, $\langle \delta V^2 \rangle$, of low-frequency unresolved transverse Alfvén waves can be derived from the measured FWHM of O IV and Si IV emission lines. These lines show nonthermally broadened profiles caused by the unresolved large-scale turbulent (nonthermal) motions of O IV and Si IV ions. In the

general case, where the nonthermal motions are assumed to be random, the observed/measured FWHMs of an optically thin emission line are given by

$$\text{FWHM} = \sqrt{\Delta \lambda_{\text{inst}}^2 + 4 \ln 2 \left(\frac{\lambda_0}{c} \right)^2 \left(\frac{2k_B T_i}{M_i} + V_{\text{turb}}^2 \right)}, \quad (3)$$

where $\Delta \lambda_{\text{inst}}$ is the instrumental broadening, λ_0 is the rest wavelength, c is the speed of light, k_B is the Boltzmann constant, T_i and M_i are the temperature and atomic mass of ion i , respectively, and V_{turb} is the nonthermal ion speed along the LOS. Here, we assume that the nonthermal motions of coronal

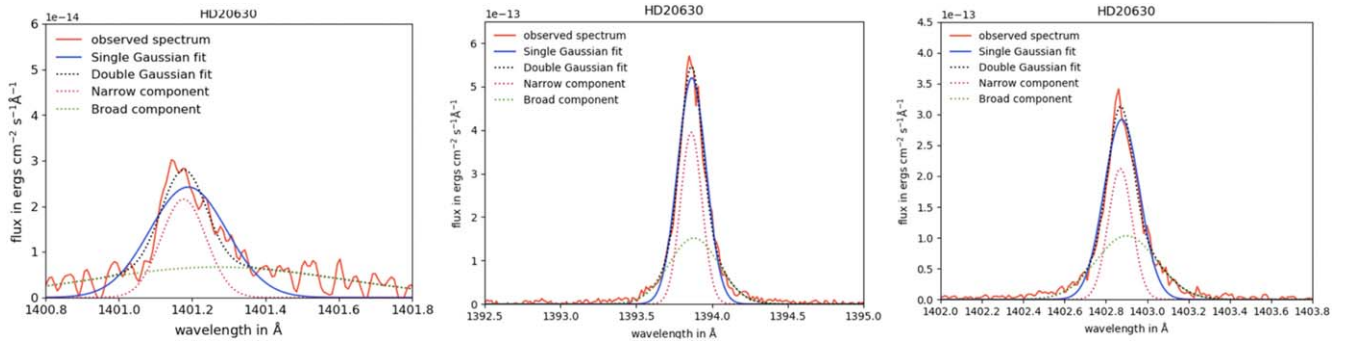


Figure 2. The profiles of O IV 1399.78, 1401, Si IV 1404, Si IV 1406 Å derived from HST/STIS observations of κ^1 Ceti.

ions are caused by the Alfvén waves, which cause the ions to move with a velocity equal to the rms wave velocity perturbation, $\sqrt{\langle \delta V^2 \rangle}$. Then, the rms wave amplitude can be derived directly from the turbulent velocity as

$$\sqrt{\langle \delta V^2 \rangle} = \frac{2V_{\text{turb}}}{|\cos \alpha|},$$

where α is the angle between the plane perpendicular to the magnetic field and the LOS vector (Hassler et al. 1990). To derive the initial amplitude of Alfvén waves at the lower boundary, we fitted the fully resolved observed profile of O IV and Si IV lines (see Figure 2) obtained with high-resolution HST/STIS observations. FWHM is derived from the narrow component of Gaussian line fits. We then subtracted the Doppler and instrumental broadening components to obtain the nonthermal broadening according to Equation (2). This results in the turbulent velocity of 24.6 km s^{-1} , which is ~ 1.6 times greater than that measured in O IV lines of the current Sun (Sokolov et al. 2013). Assigning the nonthermal line broadening to large-scale turbulent motions via unresolved Alfvén waves, we derived the average wave amplitude, $V_w = \sqrt{\langle \delta V^2 \rangle}$. Thus, in our stellar models we combined the density derived from the line ratios with this turbulent velocity to models for 2012.8 (M2012) and for 2013.7 (M2013) epochs, and we set the input normalized Poynting flux, $P_w = 26.9 P_{w0}$, where $P_{w0} = 1.1 \times 10^5 \text{ erg cm}^{-2} \text{ G}^{-1}$ is the reference-normalized solar chromospheric Alfvén wave Poynting flux, used in our current and earlier solar modeling studies (Sokolov et al. 2013; van der Holst et al. 2014; Oran et al. 2017).

3.2.3. The Coronal Structure and Emission from κ^1 Ceti

We calculated coronal models of κ^1 Ceti using the reconstructed magnetogram for the 2012.8 epoch, referred to as StellarE1, and the 2013.7 epoch, referred to as StellarE2. The left panel of Figure 3 shows the converged (steady) solution for the global magnetic coronal structure of the star at the 2012.8 epoch, which is mostly represented by a dominant dipolar field tilted at 9° (dipole strength of 15.38 G vs. 5.1 and 7.99 G for quadrupole and octupole, respectively, at 2013.7) and resembles the current Sun’s coronal state at the minimum of the solar cycle. The right panel demonstrates the magnetic field topology 11 months later, suggesting that the stellar dipole magnetic field has undergone a dramatic transition from a simple dipole to 45° tilted dipolar magnetic field, with over 2/3 of the contribution from quadrupolar and octupolar components.

This configuration is typical for the current Sun’s magnetic field at the declining phase of the solar maximum. The total unsigned open magnetic flux at the 2012.8 epoch is $6.2 \times 10^{23} \text{ Mx}$, while the flux decreases to $4.5 \times 10^{23} \text{ Mx}$ at the 2013.7 epoch.

The calculated output SXR fluxes in Fe XV 284 Å and Fe XVI 335 Å lines and the SXR band 1–8 Å from the StellarE1 and StellarE2 models are presented in Table 2. The integrated fluxes in Fe XV 284 Å and Fe XVI 335 Å emission lines during the 2012.8 epoch are 50% and 37% larger than that at 2013.7. These simulated fluxes are a factor of 5–10 smaller than measured from the EUVE observations of this star in 1995 (Ribas et al. 2005). The major reason for the underestimated flux is in the incomplete representation of the surface magnetic flux via ZDI reconstruction. As we discussed in Section 3.2.1, the stellar magnetic map geometry can only represent the large-scale magnetic structures $> 72^\circ$, and the maximum spherical harmonic expansion is $l_{\text{max}} = 5$. Such low spherical harmonic number representation of the global magnetic field misses over 10 times the total unsigned magnetic field (See et al. 2019). Indeed, measurements of κ^1 Ceti unsigned magnetic flux from Zeeman broadening of unpolarized spectra suggest an average magnetic field of $\sim 500 \text{ G}$ (Kochukhov et al. 2020), which is about 20 times greater than that inferred from ZDI maps presented in Figure 1. This is the result of an unresolved flux in Stokes V (circularly polarized) observations due to magnetic flux cancellation within pixel resolution or starspots due to suppression of the Zeeman effect in dark regions (flux cancellation of oppositely signed spots). Thus, about 95% of the magnetic flux is concentrated in smaller magnetic structures mostly represented by bipolar regions or starspot groups. To resolve such small-scale structures, high-precision photometric techniques such as transit observations by Kepler, K2, and TESS, or other photometry like Evryscope (Howard et al. 2020), are required. In the transit observations, starspots are usually identified as rotationally modulated “dips” that appear as dark regions on the stellar disk (Namekata et al. 2019). MOST observations of κ^1 Ceti taken in 2003–2005 suggest that the surface magnetic flux is mostly concentrated in two starspots in 2003 (with areas of 3.6% and 1%), three spots in 2004 (with areas of 1.9%, 9%, and 5.3%), and two spots in 2005 covering 2.9% and 2.2% of the stellar disk, respectively (Rucinski et al. 2004; Walker et al. 2007). These observations suggest that the lifetime of large spots does not exceed 1 yr and are consistent with the recent estimates of such large starspots from young solar-type stars in Kepler data (Namekata et al. 2019). This suggests that most of the magnetic flux is

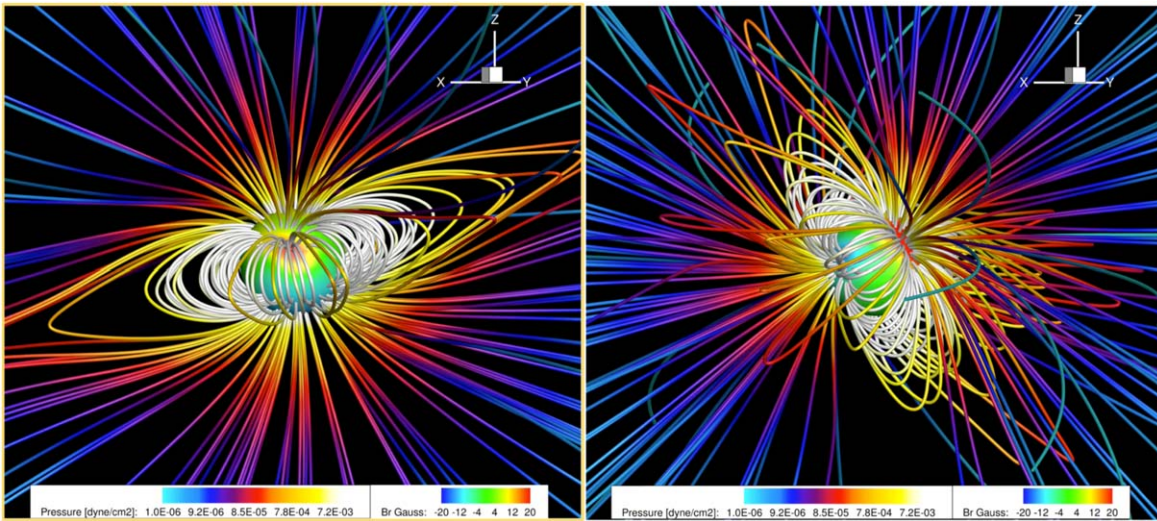


Figure 3. Global structure of the stellar magnetic corona of κ^1 Ceti at 2012.9 (left panel) and 2013.8 (right panel), with the superimposed plasma pressure along the field lines specified by the color bars.

Table 2
Summary of the Stellar Coronal Intensities and Wind Mass Fluxes from the Solar Model M0 and StellarE1 and StellarE2 Models

Star	Fe XV 284 Å ($\text{erg cm}^{-2} \text{s}^{-1}$)	Fe XVI 335 Å ($\text{erg cm}^{-2} \text{s}^{-1}$)	SXR 1–8 Å ($10^{-5} \text{erg cm}^{-2} \text{s}^{-1}$)	\dot{M} ($10^{-14} M_{\odot} \text{yr}^{-1}$)	$V_{\text{fast}}/V_{\text{slow}}$ (km s^{-1})	$P_{\text{dyn}}/P_{\text{E}}$
Sun/CR 2106 (M0)	0.014	0.005	2.7	2.86	700/450	0.7–6.6 ^a
κ^1 Ceti –2012.8 StellarE1	0.42	0.22	7000	286	1152/696	188–1379 ^a
κ^1 Ceti –2013.7 StellarE2	0.27	0.16	4500	238	1253/692	104–958 ^a

Note.

^a Dynamic pressure of the stellar wind is measured at 1 au with the minimum and maximum values around Earth’s orbit.

concentrated at angular sizes of $<16^\circ$ and thus would require the ZDI reconstruction with $l_{\text{max}} > 15$.

In order to reconcile to the total average unsigned magnetic flux measured in unpolarized observations (Kochukhov et al. 2020), we will use the MOST mission 2003–2005 data and our recent TESS Cycle 1 data of the rotational modulation of the star to characterize the starspot(s) to be added as bipoles to the ZDI magnetograms. These localized structures carry over 90% of the unsigned magnetic flux that should, therefore, provide the dominant contribution of the coronal SXR and EUV fluxes as it follows from the empirical nearly linear relationship, $F_{\text{SXR}} \propto \Phi^{1.15}$, between the stellar SXR and surface magnetic fluxes (Pevtsov et al. 2003). The estimates of the expected contribution of starspots to the overall EUV and SXR flux can be based on a “Sun-as-a-star” study of a single sunspot represented by the active region (AR 12699) transited throughout the solar disk (Toriumi et al. 2020). This transiting sunspot with the area $A = 240$ MSH (millionth of the solar hemisphere) was associated with $>10\%$ enhancement of the coronal emission in the EUV Fe XV 284 Å and Fe XVI 335 Å emission lines and SXR 1–8 Å flux by ~ 10 times the quiet Sun’s flux. We can scale the spot’s contribution to the stellar coronal emission using the κ^1 Ceti starspot areas observed with MOST from 10,000–90,000 MSH. Assuming the starspot’s magnetic field to be comparable to the sunspot’s field, we can estimate the lower bound of the magnetic flux of a starspot associated with the coronal active region, $\Phi = B_0 A$, where B is

the starspot’s magnetic field strength, to be ≥ 40 –375 times the AR 12699 flux. Then, using the solar/stellar SXR and surface magnetic fluxes, we find that the low limit of the expected contribution to the EUV and SXR stellar flux from the starspot should be >7 –90 times the quiescent (unspotted) area of the star modeled here. We will study these contributions using the MHD model of the star in the upcoming study.

We used the CHIANTI code to construct the 3D synthetic coronal emission maps of κ^1 Ceti at two epochs, 2012 August (2012.8) and 2013 July (2013.7). The 2D slices of the 3D coronal images of κ^1 Ceti are presented in Figure 4. The top panel of the figure shows the X-ray- and EUV-emitting regions of the corona at 2012.8 of the star in the mid- to higher northern latitudes and the well-pronounced coronal hole formed around the southern pole of the star. However, the coronal flux becomes significantly different 11 months later as the magnetic dipole flips, exposing the bright X-ray-to-EUV-emitting corona with 40% less flux due to the stronger disorganized field (less closed magnetic flux) in the southern to midlatitudes of the star and the formation of the coronal hole appearing in the northern regions of the star. We used these data to calculate the volumetric emission measure, $\text{VEM} = n_e n_i V$ (n_e , n_i are the electron and ion number densities, V is the volume of emitting plasma), distribution over temperatures. Figure 5 shows the simulated VEM distribution of the solar corona (black line) and the stellar corona at 2012.8 (red line) and 2013.7 (blue line), with the dominant contribution at 6.3 MK, which is consistent

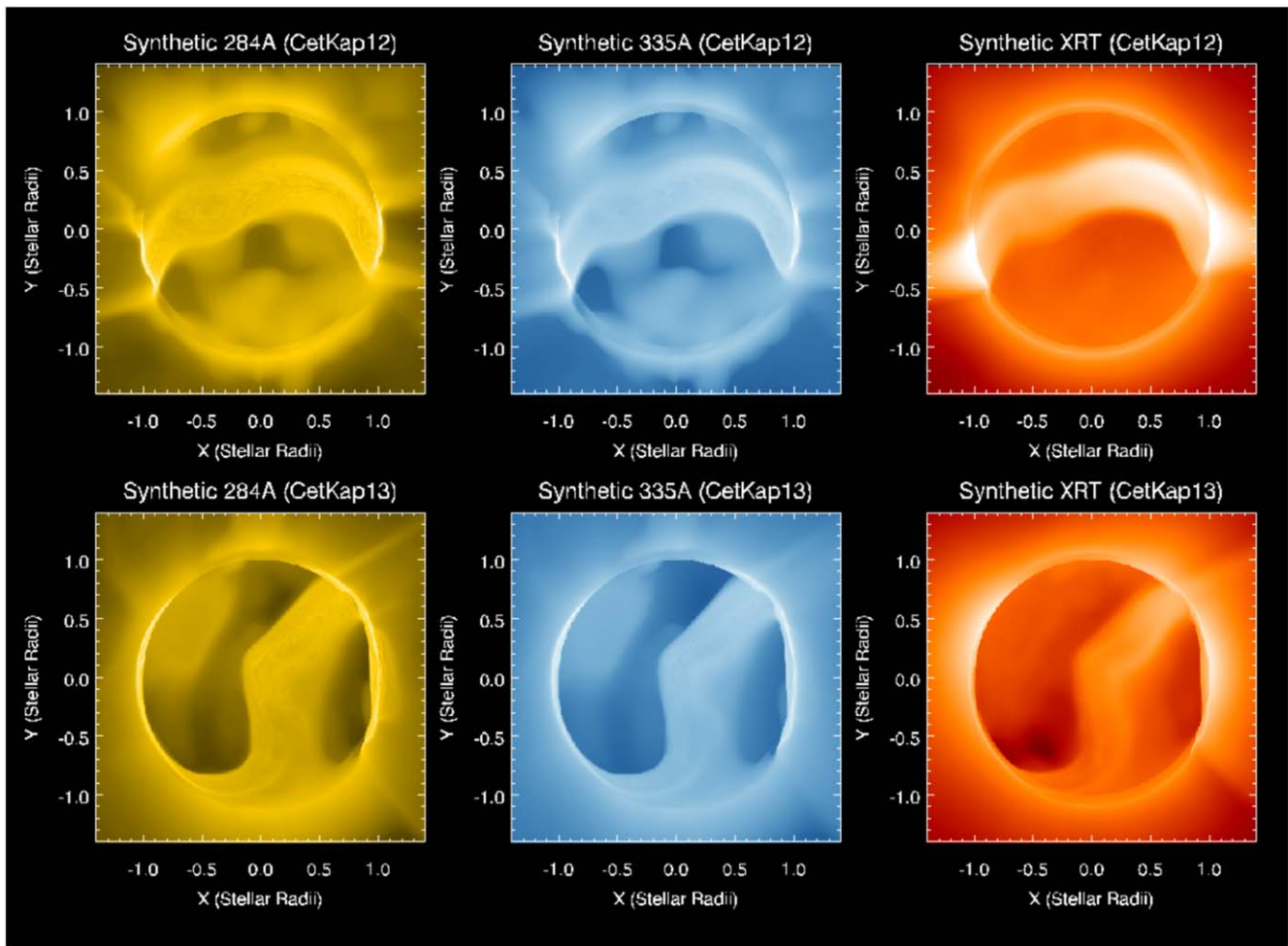


Figure 4. The coronal images of the Sun (top row and at 2012.9) and the 2013.8 epoch (bottom row) at 284 Å, 335 Å, and the Hinode X-Ray Telescope band.

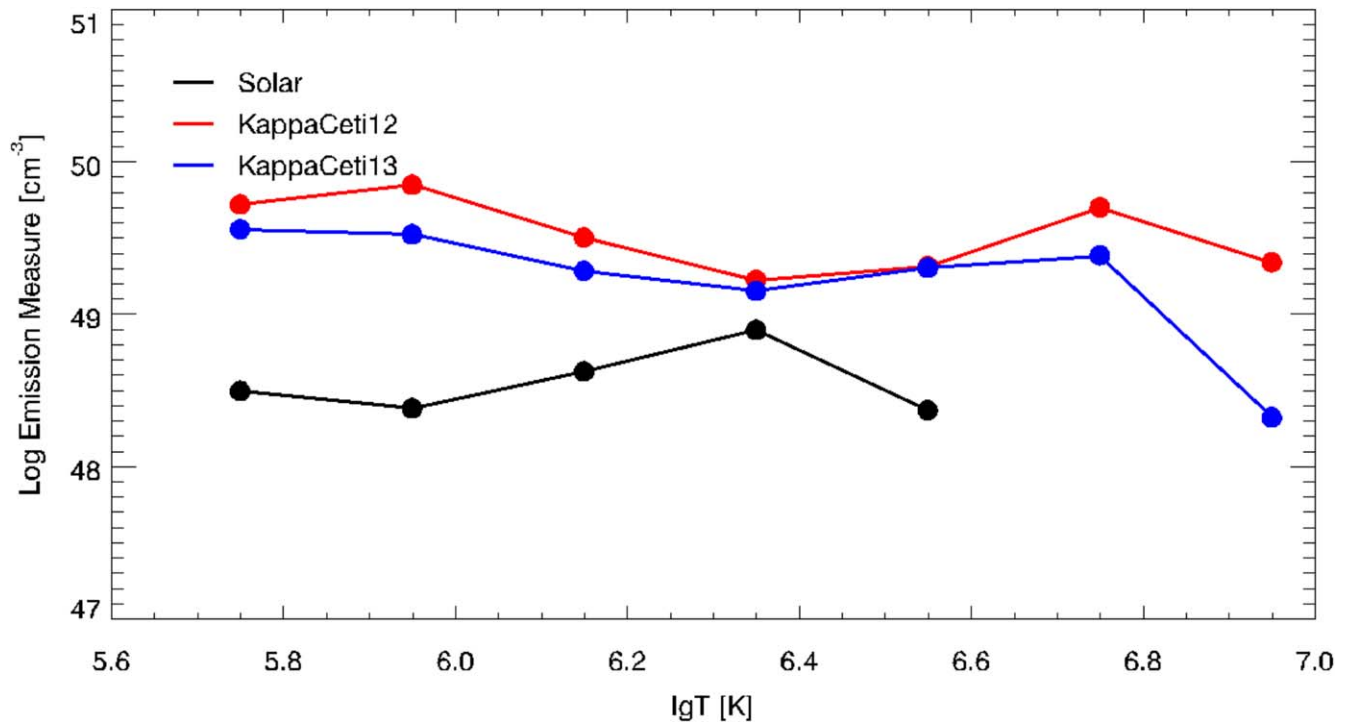


Figure 5. VEM distribution over temperature for the Sun (black) and κ^1 Ceti at the 2012.8 (red) and 2013.7 epochs (blue).

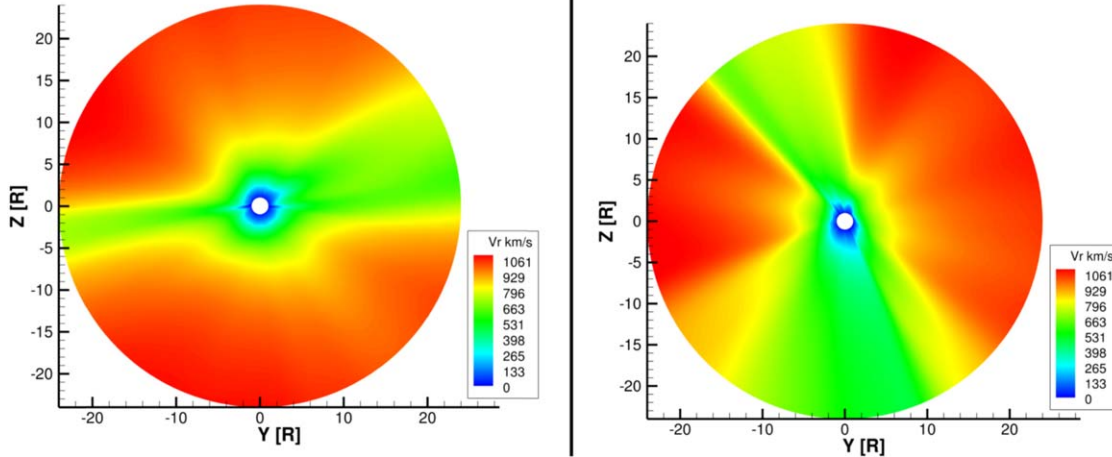


Figure 6. The 2D Y - Z maps (at the ecliptic plane, $X = 0$) of the radial velocity of κ^1 Ceti’s (in km s^{-1}) over the first 24 stellar radii at 2012.8 (left panel) and 2013.7 (right panel).

with the XMM-Newton spectra of the star (Telleschi et al. 2005). It is evident that the weakening of the dipole field and appearance of multipole components reduced the VEM at this temperature by a factor of 2.5, with the maximum temperature at ~ 6 MK.

3.2.4. The Stellar Wind from κ^1 Ceti

A. Mass-loss Rates. Our AWSOM model produces steady wind solutions for the 2012.8 and 2013.7 epochs. The global wind shows the two-component stellar wind of κ^1 Ceti. The plasma accelerated from giant coronal holes (see Figure 4) is driven by the Alfvén wave ponderomotive force, while the slow wind is formed owing to the thermal pressure gradient. At the 2012.8 epoch, the fast wind reaches its terminal velocity of 1152 km s^{-1} within the first $15 R_{\text{star}}$, while the slow and dense component of the wind originates from the regions associated with the equatorial streamer belt structures at 696 km s^{-1} . Once the steady solution for the coronal density, magnetic field, and velocity is obtained, we calculated the mass-loss rate as

$$\dot{M} = \int_A \rho \mathbf{v} \cdot d\mathbf{A}.$$

The simulated stellar wind density is ~ 50 – 100 times greater than that of the current Sun’s wind and faster by a factor of 2, which produces a massive wind with a mass-loss rate of $2.8 \times 10^{-12} M_{\odot}$, which is 100 times greater than that observed from the current Sun. Our wind simulations are consistent with the empirically derived scaling of the mass-loss rates with the SXR surface fluxes, $\dot{M} \propto F_X^{1.34}$, which provides the upper bound of mass-loss rate of a young G-type star with the surface X-ray flux of $10^6 \text{ erg cm}^{-2} \text{ s}^{-1}$ that is representative of κ^1 Ceti (Wood et al. 2014). However, this rate is twice as large as that obtained in the polytropic solutions of Airapetian & Usmanov (2016) and Do Nascimento et al. (2016). We also find that the mass-loss rate responds to the change of the large-scale magnetic structures at the 2013.7 epoch with 17% less mass-loss rate. The resulting 2D (X - Y at $Z = 0$, the ecliptic plane) maps of the wind radial velocity, V_r , from its base to 1 to 24 R_{\odot} at two epochs in the StellarE1 model are presented in

Figure 6. Figure 6 shows that the radial stellar wind velocity of the slow and fast components are 1152 km s^{-1} and 696 km s^{-1} , respectively, for 2012.8 epoch (the left panel of Figure 6). The slow wind propagates out along the astrospheric current sheet or in the plane slightly ($\sim 9^\circ$) tilted to the ecliptic plane, while the fast wind propagation is associated with the magnetically open (coronal hole) regions. The geometry of the stellar wind components drastically changes 11 months later (the right panel of Figure 6) as the global stellar magnetic field and associated astrospheric current sheet becomes tilted by 45° (see Figure 3). The slow and fast wind components do not change significantly reaching 692 km s^{-1} and 1253 km s^{-1} , respectively, but the total mass loss rate drops by $\sim 17\%$.

Our earlier sensitivity studies have shown that the wind mass-loss rate increases about linearly with the input Alfvén wave Poynting flux (Boro Saikia et al. 2020). Such linear scaling can be explained due to the dissipation of the enhanced Alfvén wave flux that produces the greater thermal pressure gradient. This causes larger acceleration of the slow wind from equatorial streamers, while the fast component of the wind is formed due to the plasma acceleration via the magnetic pressure gradient of Alfvén waves.

B. Corotating Interaction Regions. Our steady wind solutions for κ^1 Ceti also show (see left and right panels of Figure 7) the formation of well-pronounced regions of enhanced density of the stellar wind at two epochs, 2012.8 and 2013.7. These structures are the stellar wind stream interaction regions (SIRs) formed as a result of the interaction of a stream of high-speed solar wind originating in the stellar coronal hole structures (see Figure 4), with the preceding slower wind formed along the equatorial regions of the stellar corona. The interaction of these streams forms a region of compressed plasma, SIR, along the leading edge of the stream, which, due to the rotation of the star at 9.2 days, is twisted approximately into an Archimedean (or Parker 1958) spiral. Because the coronal holes may persist for many months, the interaction regions and high-speed streams tend to sweep past an exoplanet at regular intervals of approximately half of the stellar rotation period (~ 4.6 days) forming CIRs along the Parker spirals. These regions are signified by the compression

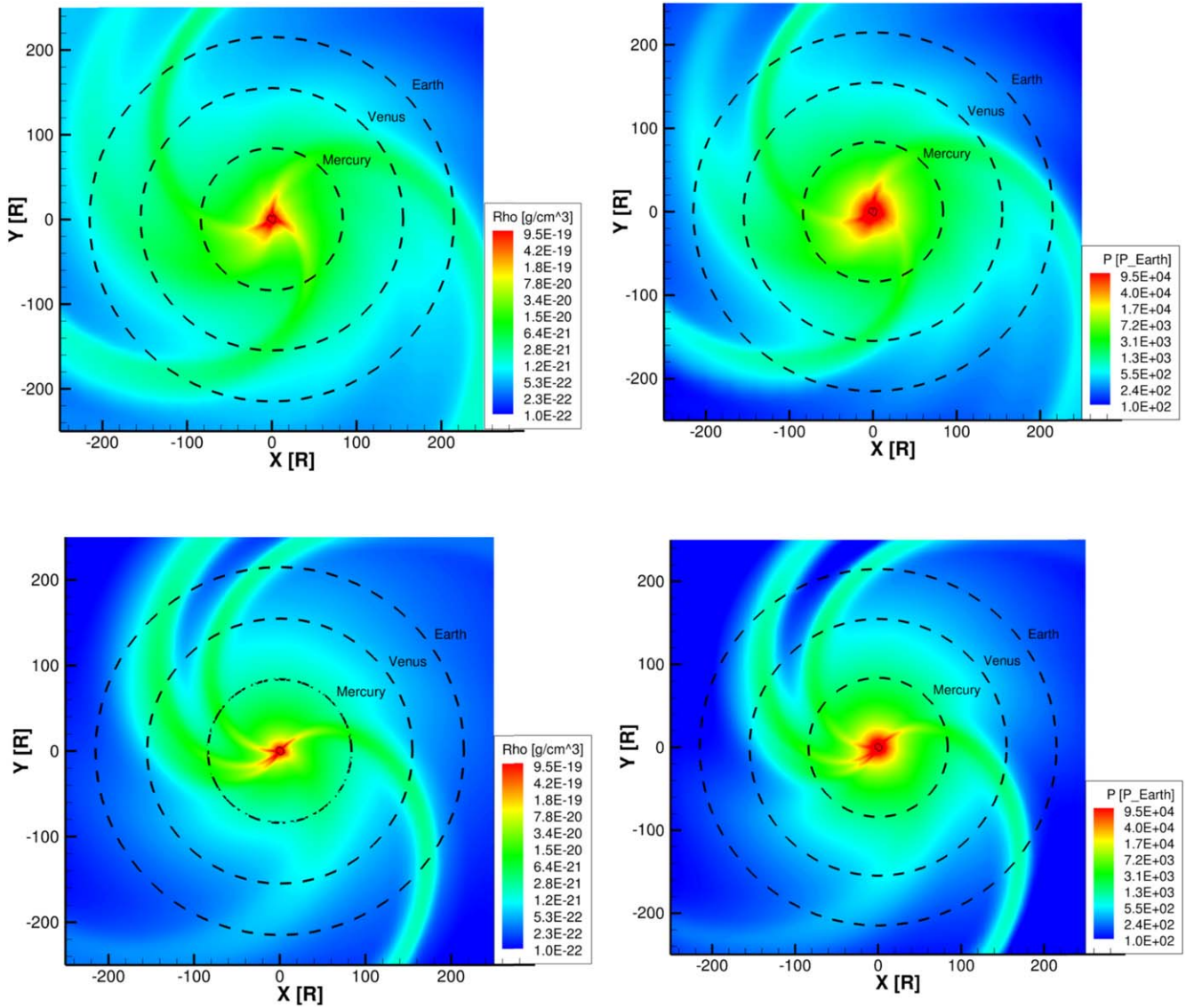


Figure 7. Top panel: 2D slice of the X - Y plane ($Z = 0$) of the plasma density and the dynamic pressure of CIRs from κ^1 Ceti formed at the 2012.8 epoch (left) and 2013.7 epoch (right). Black dashed lines show the orbits of Mercury, Venus, and Earth.

region ahead of the fast wind and rarefaction region behind it that remain stationary in a frame corotating with the Sun shown in Figure 7. Due to the much larger difference between the fast and slow wind components than that of the current Sun, its compression regions steepen into strong shocks propagating at $>1000 \text{ km s}^{-1}$ at orbital locations of Mercury (0.4 au), Venus (0.7 au), and Earth (1 au).

Figure 7 shows that stellar CIR plasma densities at $10 R_{\odot}$ (0.05 au) and $216 R_{\odot}$ (1 au) are $5 \times 10^5 \text{ cm}^{-3}$ and $2 \times 10^3 \text{ cm}^{-3}$, respectively. These stellar wind densities are a factor of 300 greater than the solar wind’s density measured by Parker Solar Probe (Kim et al. 2020). These results are important, as they provide the quantitative characterization of physical conditions at orbital distances of close-in exoplanets around G- and K-type stars, including eps Eri b (Benedict et al. 2006), K2-229b (Santerne et al. 2018), K2-198b,c, K2-168b,c (Hedges et al. 2019), and HD 189733b (Barth et al. 2021). The simulated dynamic pressure exerted by CIRs at close-in exoplanets reaches 50,000–10,000 times greater at 0.05 au and 1300 times greater at 1 au than that exerted to the

magnetosphere of the current Earth. The standoff distance of the stellar wind to the planet, R_{sub} , can be found from the balance between the dynamic pressure, $P_d = \rho v^2$, of the stellar wind and the magnetospheric pressure, P_m , of the dipolar planetary field as (Beard 1960)

$$R_{\text{sub}} \propto P_d^{1/6}.$$

This relation suggests that the dynamic pressure from stellar CIRs would compress the magnetospheres of Earth-like exoplanets (at the current Earth’s magnetic moment) to the standoff distance of $\sim 3 R_{\oplus}$ and thus ignite strong geomagnetic currents in the early Earth atmosphere. It is interesting that Carrington-type coronal mass ejections (CMEs) modeled in Airapetian et al. (2016) can provide the comparable magnetospheric compression that will open up to 60% of Earth’s geomagnetic field.

Figure 8 shows the enhancement of the plasma density in CIR-driven shock up to 2000 cm^{-3} , which is a factor of 100 greater than the CIR’s density from the current Sun. The total

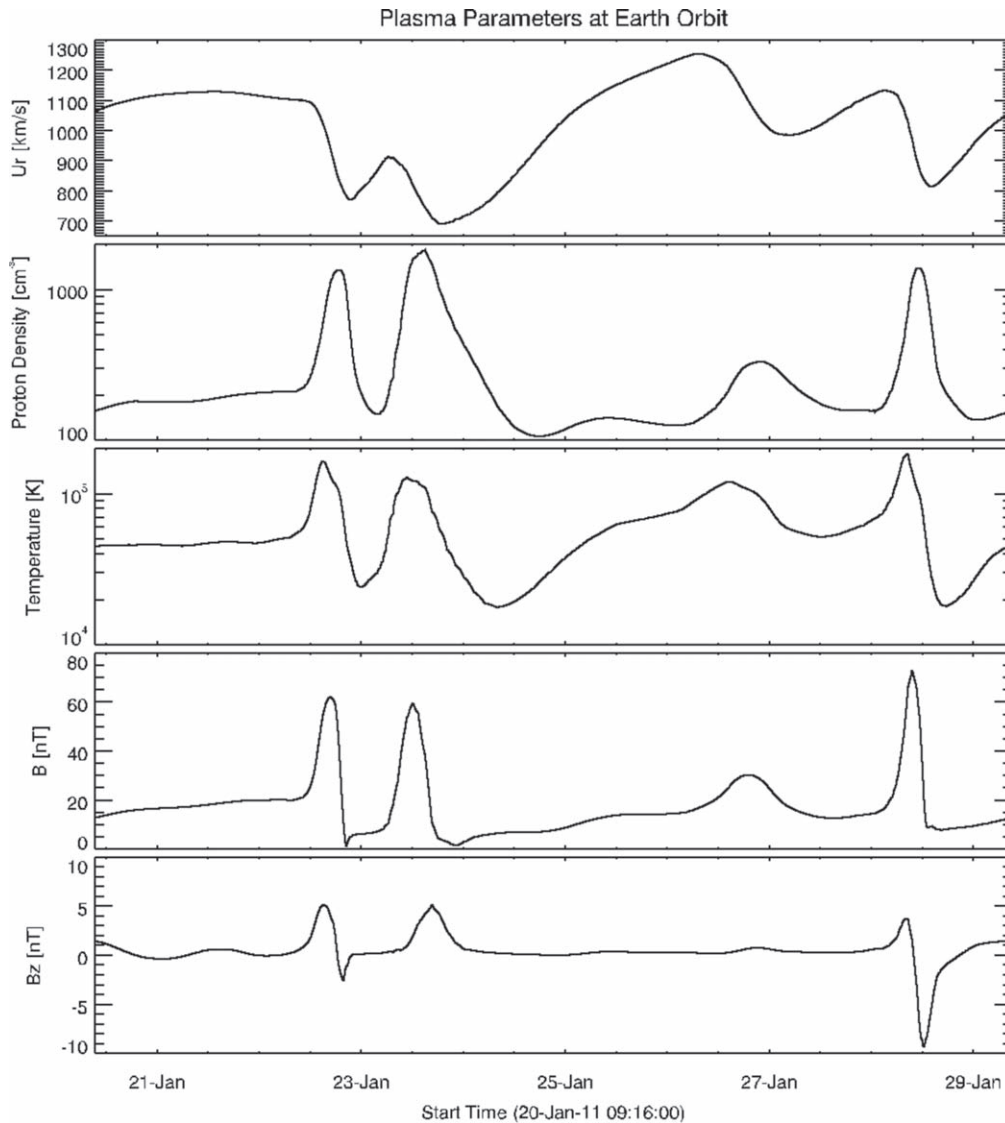


Figure 8. The physical properties of the stellar CIR (2012.8 epoch) at Earth orbit: top to bottom panels represent the radial velocity (in km s^{-1}), proton density (in cm^{-3}), temperature (in K), and magnetic field (in nT).

magnetic field reaches 80 nT, with the B_z component of magnetic field of -10 nT, which is comparable to the values measured in solar CMEs introducing magnetic storms in Earth’s geospace (from magnetosphere to the middle atmosphere; Yurchyshyn et al. 2005; Li et al. 2018). The southward magnetic field of an CIR undergoes reconnection with the exoplanetary magnetic field and further pushes the magnetosphere close to the planet and opening the polar cap to a larger degree. We will study these geomagnetic field scenarios of interactions of stellar CIR-driven shocks with Earth-like and giant exoplanets in our future studies. It is important to note that while these dense shocked regions can be important contributors to the transient magnetospheric compression of exoplanets, their contribution to the overall mass-loss rate is small (a few percent of the stellar wind mass loss) because of their compact cross-section areas.

Stellar CIR-driven shock will also drive acceleration of energetic electrons and protons similar to solar CIRs (Richardson 2018). In our simulations, they represent quasi-steady state structures interacting with magnetospheres of early

Venus, Earth, and exoplanets every 4.6 days. Such shocks can produce energized seed particle populations (up to a few tens of MeV) that will enhance SEP production by CME-driven shocks. As these particles penetrate into $\text{N}_2\text{-CO}_2$ rich atmospheres with trace amounts of methane and water vapor, they can ignite the formation of complex molecules in mildly reducing atmospheres of early Earth and Earth-like exoplanets, including hydrogen cyanide and formaldehyde, the precursors of proteins, complex sugars, and building blocks of nucleobases (Patel et al. 2015; Airapetian et al. 2016, 2020; Rimmer & Rugheimer 2019; Fu et al. 2019).

4. Conclusions

Here, we expanded the AWSoMstellar coronal model used previously to model stellar coronal environments by Alvarado-Gómez et al. (2016a, 2016b) and Boro Saikia et al. (2020). These models utilized ZDI magnetograms of active stars but did not use the constrained inputs for the thermodynamics of the stellar corona. Here, we used the fully thermodynamic

MHD equations with the coronal heating source via input Alfvén wave energy flux specified at the upper chromosphere and constrained by HST/STIS observations of κ^1 Ceti. Thus, for the first time we have simulated the stellar corona as the full solution of the MHD chromospheric model. We also calculated the solar corona at CR 2106 to check that the model produces coronal and wind mass fluxes consistently with observations and for comparison with stellar models.

Our models find that the dominant dipole magnetic field derived from ZDI magnetic magnetograms of the star and the dissipation of the Alfvén wave energy flux specified by the HST/STIS data produce a hot (6 MK) corona, which is consistent with the observationally derived EM distribution from EUVE data (Telleschi et al. 2005). However, the EUV fluxes appear to be 5–10 times smaller than observed fluxes. We suggested that this discrepancy can be attributed to the missing magnetic flux in small-scale magnetic structures associated with starspots to be added in the upcoming study. We also find that the global magnetic field of the star undergoes a transition to a tilted weaker dipole with developed multipole components 11 months later. This disorganized magnetic field produces the stellar corona at 6.3 MK, but with 40% less EUV coronal fluxes. The simulated mass-loss rate from κ^1 Ceti at the 2012.8 epoch appears to be 100 times greater than the mass-loss rate observed from the current Sun’s wind. We find that the weaker dipoled field at the 2013.7 epoch produces the reduction of the mass-loss rate by 40%.

A new structure simulated in our model is the stellar CIR resulting from the interaction of fast and slow winds that has a dynamic pressure over 1380 times greater than that formed in the CIRs from the current Sun. This is a very important result, as CIRs cause magnetic storms on Earth (Maggiolo et al. 2017; Richardson 2018). The initiation of magnetic storms is associated with enhanced dynamic pressure that compresses Earth’s magnetosphere, causes the induction of ionospheric currents, and results in Joule heating of the ionospheric and thermospheric layers of the planet. The enhanced magnetic field with the B_z component reaching 80 nT in our simulations is comparable to the magnetic fields of strongest CMEs. Such a strong southward field can ignite magnetic reconnection with the (exo)planetary magnetospheric field and thus produce strong fluxes of precipitating electrons and protons into the upper atmosphere, provoking additional heating and associated enhanced (with respect to the EUV-driven escape) escape rates. These processes can be crucial in evaluating the magnetospheric states of exoplanets around active stars because induced current dissipation will enhance the atmospheric escape from Earth-like exoplanets around active stars and can be critical for habitability conditions for rocky exoplanets in close-in habitable zones around red dwarfs (Cohen et al. 2014; Dong et al. 2018; Airapetian et al. 2020). We should note that these processes can produce energized seed particle populations (up to a few tens of MeV) that will enhance SEP production by CME-driven shocks. (Lugaz et al. 2015; Airapetian et al. 2020).

Thus, our MHD model provides the framework to realistically model coronal environments of solar-like planet hosts by applying the data-constrained setup developed for κ^1 Ceti to other young stars, specifically EK Dra, the “infant” proxy of our Sun at 100 Myr, younger solar-like (T Tau) stars at <10 Myr, and active K and M dwarfs. In conclusion, we

should mention that the presented model accounts for the coronal heating in the closed magnetic loops only via Alfvén wave energy dissipation. However, recent high-resolution observations of solar coronal loops suggest that some portion of the heating can be explained via explosive reconnection events known as nanoflares. In the future developments of this tool, we will introduce a heating term via nanoflares that contribute to the coronal loop and coronal background heating (Chitta et al. 2018; Bahaiddin et al. 2020).

Our data-driven MHD models can provide predictive capabilities for SXR and EUV intensities and the wind mass fluxes from young G, K, and M planet hosts with constrained inputs supplied by TESS, HST, XMM-Newton, NICER, and ground-based facilities. The rotational modulation of the optical flux with TESS and other facilities will provide the starspot(s) size and its (their) locations that will be added to the ZDI magnetogram to account for the observed total unsigned magnetic flux. These reconstructions will be used to compare against observationally derived EUV fluxes (stars observed by EUVE observatory) and/or using their Far-UV proxies (France et al. 2018). Thus, a coordinated multi-observatory campaign to address the stellar space weather environments is required to assess the habitability conditions of Earth-like planets around young Sun-like (G and K type) and M dwarfs. The first phase of the observational campaign “Evolving Magnetic Lives of Young Suns” has been recently started to characterize coronae, winds, and superflares from young solar-like planet-hosting stars (Soderblom et al. 2019).

V.S.A. was supported by NASA Exobiology grant No. 80NSSC17K0463, TESS Cycle 1, HST Cycle 27, and NICER Cycle 2 grants. M.J. acknowledges support from NASA’s SDO/AIA (NNG04EA00C) contract to the LMSAL. O.K. acknowledges support by the Swedish Research Council, the Swedish National Space Agency, and the Royal Swedish Academy of Sciences. The observations that support the findings of this study were obtained as a part of spectropolarimetric observations, previously obtained HST/STIS, MOST, and TESS, as well as XMM-Newton observations of κ^1 Ceti. The data are available in the public archive at <https://mast.stsci.edu/portal/Mashup/Clients/Mast/Portal.html>. This modeling work was performing by applying the SWMF/BATSRUS tools developed at the University of Michigan Center for Space Environment Modeling (CSEM) and made available through the NASA Community Coordinated Modeling Center (CCMC). Resources supporting this work were provided by the NASA High-End Computing (HEC) Program through the NASA Advanced Supercomputing (NAS) Division at Ames Research Center. Simulations were performed on NASA’s HECC Pleiades cluster.

ORCID iDs

Vladimir S. Airapetian  <https://orcid.org/0000-0003-4452-0588>

Meng Jin  <https://orcid.org/0000-0002-9672-3873>

Oleg Kochukhov  <https://orcid.org/0000-0003-3061-4591>

Manuel Güdel  <https://orcid.org/0000-0001-9818-0588>

Bart Van Der Holst  <https://orcid.org/0000-0001-5260-3944>

W. Manchester IV  <https://orcid.org/0000-0003-0472-9408>

References

- Airapetian, V., & Usmanov, A. 2016, *ApJL*, 817, L24
- Airapetian, V. S. 2017, in *Extreme Events in Geospace: Origins, Predictability, and Consequences*, ed. N. Buzulukova (Amsterdam: Elsevier), 611
- Airapetian, V. S., Barnes, R., Cohen, O., et al. 2020, *IJASB*, 19, 136
- Airapetian, V. S., Carpenter, K. G., & Ofman, L. 2010, *ApJ*, 723, 1210
- Airapetian, V. S., & Cuntz, M. 2015, *Atmospheric Heating and Wind Acceleration, in Giants of Eclipse: The ζ Aurigae Stars and Other Binary Systems*, 408 (Switzerland: Springer International Publishing), 123, Ch. 5
- Airapetian, V. S., Glocer, A., Gronoff, G. E., Hébrard, E., & Danchi, W. 2016, *NatGe*, 9, 452
- Airapetian, V. S., Glocer, A., Khazanov, G. V., et al. 2017, *ApJL*, 836, L3
- Airapetian, V. S., Ofman, L., Robinson, R. D., & Davila, J. 2000, *ApJ*, 528, 965
- Alvarado-Gómez, J. D., Hussain, G. A. J., Cohen, O., et al. 2016a, *A&A*, 588, A28
- Alvarado-Gómez, J. D., Hussain, G. A. J., Cohen, O., et al. 2016b, *A&A*, 594, A95
- An, C.-H., Suess, S. T., Moore, R. L., & Musielak, Z. E. 1990, *ApJ*, 350, 309
- Bahaudin, S. M., Bradshaw, S. J., & Winebarger, A. R. 2020, *NatAs*, 5, 237
- Banerjee, D., Pérez-Suárez, D., Doyle, J. G., et al. 2009, *A&A*, 501, L15
- Barth, P., Helling, Ch., Stüeken, E. E., et al. 2021, *MNRAS*, 502, 6201
- Beard, D. B. 1960, *JGR*, 65, 3559
- Benedict, G. F., McArthur, B. E., Gatewood, G., et al. 2006, *AJ*, 132, 2206
- Boro Saikia, S., Jeffers, S. V., Petit, P., et al. 2015, *A&A*, 573, A17
- Boro Saikia, S., Jin, M., Johnstone, C. P., et al. 2020, *A&A*, 635, A178
- Brun, A. S., & Browning, M. K. 2017, *LRSP*, 14, 4
- Carpenter, K. G., Robinson, R. D., & Judge, P. G. 1995, *ApJ*, 444, 424
- Chen, C. H. K., Bale, S. D., Bonnell, J. W., et al. 2020, *ApJS*, 246, 53
- Chitta, L. P., Peters, H., & Solanki, S. K. 2018, *A&A*, 615, L9
- Cnossen, I., Sanz-Forcada, J., Favata, F., et al. 2007, *JGR*, 112, E2008
- Cohen, O., Sokolov, I. V., Roussev, I. I., & Gombosi, T. I. 2008, *JGR*, 113, A03104
- Cohen, O., Drake, J. J., Glocer, A., et al. 2014, *ApJ*, 790, 57
- Cohen, O., Glocer, A., Garraffo, C., et al. 2018, *ApJL*, 856, L11
- Cranmer, S. R., & Saar, S. H. 2011, *ApJ*, 741, 54
- Cranmer, S. R., Asgari-Targhi, M., Miralles, M. P., et al. 2015, *RSPTA*, 373, 20140148
- Cranmer, S. R., & Winebarger, A. R. 2019, *ARA&A*, 57, 157
- Cuntz, M., & Guinan, E. 2016, *ApJ*, 827, 79
- Dahlburg, R. B., Einaudi, G., Taylor, B. D., et al. 2016, *ApJ*, 817, 47
- De Pontieu, B., McIntosh, S. W., Carlsson, M., et al. 2007, *Sci*, 318, 1574
- Dere, K. P., Landi, E., Mason, H. E., Monsignori Fossi, B. C., & Young, P. R. 1997, *A&AS*, 125, 149
- Do Nascimento, J.-D., Jr., Vidotto, A. A., Petit, P., et al. 2016, *ApJL*, 820, L15
- Donati, J.-F., Semel, M., Carter, B. D., Rees, D. E., & Cameron, A. C. 1997, *MNRAS*, 291, 658
- Dong, C. F., Jin, M., Lingam, M., et al. 2018, *PNAS*, 115, 260
- Duvvuri, G. M., Pineda, S. J., Berta-Thompson, Z. K., et al. 2021, *ApJ*, 913, 40
- Fichtinger, B., Güdel, M., Mutel, R. L., et al. 2017, *A&A*, 599, A127
- France, K., Arulanantham, N., Fossati, L., et al. 2018, *ApJS*, 239, 16
- Fu, S., Jiang, J., Airapetian, V., et al. 2019, *ApJL*, 878, L36
- Gallet, F., Charbonnel, C., Amard, L., et al. 2017, *A&A*, 597, A14
- Garraffo, C., Drake, J. J., & Cohen, O. 2016, *ApJ*, 833, L4
- Garcia-Sage, K., Glocer, A., Drake, J. J., et al. 2017, *ApJL*, 844, L13
- Grant, S. D. T., Jess, D. B., Zaqarashvili, T. V., et al. 2018, *NatPh*, 14, 480
- Güdel, M. 2007, *LRSP*, 4, 3
- Güdel, M. 2020, *SSRv*, 216, 143
- Güdel, M., Guinan, E. F., & Skinner, S. L. 1997, *ApJ*, 483, 947
- Gustafsson, B., Edvardsson, B., Eriksson, K., et al. 2008, *A&A*, 486, 951
- Hahn, M., & Savin, D. S. W. 2013, *ApJ*, 776, 78
- Hassler, D. M., Rottman, G. J., Shoub, E. C., & Holzer, T. E. 1990, *ApJ*, 348, L77
- Hedges, C., Saunders, N., Barentsen, G., et al. 2019, *ApJL*, 880, L5
- Heinemann, M., & Olbert, S. 1980, *JGR*, 85, 1311
- Howard, W. S., Corbett, H., Law, N. M., et al. 2020, *ApJ*, 895, 140
- Huang, Y., Richmond, A. D., Deng, Y., & Roble, R. 2016, *JGR*, 117, A08334
- Jardine, M., & Collier Cameron, A. 2019, *MNRAS*, 482, 2853
- Jess, D. B., Mathioudakis, M., & Erdélyi, R. 2009, *Sci*, 323, 1582
- Jin, M., Manchester, W. B., van der Holst, B., et al. 2012, *ApJ*, 745, 6
- Jin, M., Manchester, W. B., van der Holst, B., et al. 2017, *ApJ*, 834, 173
- Johnstone, C. 2020, *ApJ*, 890, 79
- Johnstone, C., Khodachenko, M., Lüftinger, T., et al. 2019, *A&A*, 624, L10
- Johnstone, C. P., Jardine, M., & Gregory, S. G. 2014, *MNRAS*, 437, 3202
- Kawaler, S. D. 1988, *ApJ*, 333, 236
- Kim, T. K., Pogorelov, N. V., Arge, C. N., et al. 2020, *ApJS*, 246, 40
- Klimchuk, J. A. 2006, *SoPh*, 234, 41
- Kochukhov, O., Hackman, T., & Lehtinen, J. J. 2020, *A&A*, 635, 142
- Kochukhov, O., Lüftinger, T., Neiner, C., Alecian, E., & MiMes Collaboration 2014, *A&A*, 565, A83
- Kochukhov, O., Makaganiuk, V., & Piskunov, N. 2010, *A&A*, 524, A5
- Lehmann, L. T., Hussain, G. A. J., Jardine, M. M., Mackay, D. H., & Vidotto, A. A. 2019, *MNRAS*, 483, 5246
- Li, Y., Luhmann, L. J. G., & Lynch, B. J. 2018, *SoPh*, 293, 135
- Lionello, R., Linker, A., & Mikić, Z. 2009, *ApJ*, 690, 902
- Lugaz, N., Farrugia, C. J., Huang, C.-L., & Spence, H. E. 2015, *GeoRL*, 42, 4694
- Lynch, B. J., Airapetian, V. S., DeVore, C. R., et al. 2019, *ApJ*, 880, 97
- Maehara, H., Shibayama, T., Notsu, S., et al. 2012, *Natur*, 485, 478
- Maggiolo, R., Hamrin, M., De Keyser, J., et al. 2017, *JGRA*, 122, 109, 11
- Magyar, N., & Nakariakov, V. 2020, *ApJ*, 907, 55
- Mathioudakis, M., Jess, D. B., & Erdélyi, R. 2013, *SSRv*, 175, 1
- Messina, S., & Guinan, E. F. 2002, *A&A*, 393, 225
- Messina, S., & Guinan, E. F. 2003, *A&A*, 409, 1017
- McIntosh, S. W., De Pontieu, B., Carlsson, M., et al. 2011, *Natur*, 475, 477
- Mishra, W., Srivastava, N., Wang, Y., et al. 2019, *MNRAS*, 486, 4671
- Morin, J., Donati, J.-F., Petit, P., et al. 2010, *MNRAS*, 407, 2269
- Namekata, K., Maehara, H., Notsu, Y., et al. 2019, *ApJ*, 871, 187
- Notsu, Y., Maehara, H., Honda, S., et al. 2019, *ApJ*, 876, 58
- Ó Fionnagáin, D., Vidotto, A. A., & Petit, P. 2019, *MNRAS*, 487, 3079
- Ofman, L. 2010, *LRSP*, 7, 4
- Oran, R., van der Holst, B., Landi, E., et al. 2013, *ApJ*, 778, 176
- Oran, R., Landi, E., van der Holst, B., Sokolov, I. V., & Gombosi, T. I. 2017, *ApJ*, 845, 98
- Parker, E. N. 1958, *ApJ*, 128, 664
- Parker, E. N. 1972, *ApJ*, 174, 499
- Parker, E. N. 1988, *ApJ*, 330, 474
- Patel, B. H., Percivalle, C., Ritson, D. J., Duffy, C. D., & Sutherland, J. D. 2015, *NatCh*, 7, 301
- Peter, H. 2006, *A&A*, 449, 759
- Pevtsov, A. A., Fisher, G. H., Acton, L. W., et al. 2003, *ApJ*, 598, 1387
- Polito, V., Del Zanna, G., Dudik, J., et al. 2016, *A&A*, 594, A64
- Reiners, A., & Basri, G. 2006, *ApJ*, 644, 497
- Ribas, I., Guinan, E. F., Güdel, M., et al. 2005, *ApJ*, 622, 680
- Ribas, I., Porto de Mello, G. F., Ferreira, L. D., et al. 2010, *ApJ*, 714, 384
- Richardson, I. 2018, *LRSP*, 15, 1
- Rimmer, P. B., & Rugheimer, S. 2019, *Icar*, 329, 124
- Rosén, L., Kochukhov, O., Hackman, T., & Lehtinen, J. 2016, *A&A*, 593, A35
- Rucinski, S., Walker, G. A. H., Matthews, J. M., et al. 2004, *PASP*, 116, 1093
- Saar, S. H., & Baliunas, S. L. 1992, in *ASP Conf. Ser. 27, The Solar Cycle, Proceedings of the NSO/Sac Peak 12th Summer Workshop (Fourth Solar Cycle Workshop)*, ed. K. L. Harvey (San Francisco, CA: ASP), 197
- Sabri, S., Farahani, S. V., Ebadi, H., et al. 2020, *NatSR*, 10, 15603
- Sakurai, T. 1985, *A&A*, 152, 121
- Santerne, A., Brugger, B., Armstrong, D. J., et al. 2018, *NatAs*, 2, 393
- Sanz-Forcada, J., Micela, G., Ribas, I., et al. 2011, *A&A*, 532, A6
- Sanz-Forcada, J., Stelzer, B., Coffaro, M., Raetz, S., & Alvarado-Gómez, J. D. 2019, *A&A*, 631, A45
- Schaefer, B. E., King, J. R., & Deliyannis, C. P. 2000, *ApJ*, 529, 1026
- Schrijver, C. J., & De Rosa, M. L. 2003, *Sol. Phys.*, 212, 165
- See, V., Matt, S. P., Folsom, C. P., et al. 2019, *ApJ*, 876, 118
- Shoda, M., Chandran, B. D., & Cranmer, S. R. 2021, *ApJ*, 915, 52
- Soderblom, D. R., Airapetian, V. S., France, K., & Güdel, M. 2019, *The Evolving Magnetic Lives of Young Suns*, HST Proposal, Cycle 27, ID. #15825
- Sokolov, I. V., van der Holst, B., Oran, R., et al. 2013, *ApJ*, 764, 23
- Squire, J., Chandran, B. D. G., & Meyrand, R. 2020, *ApJL*, 891, L2
- Suzuki, T. K., & Inutsuka, S.-I. 2006, *ApJL*, 646, L89
- Telleschi, A., Güdel, M., Briggs, K., et al. 2005, *ApJ*, 622, 653
- Tomczyk, S., McIntosh, S. W., Keil, S. L., et al. 2007, *Sci*, 317, 1192
- Toriumi, S., Airapetian, V. S., Hudson, H. S., et al. 2020, *ApJ*, 902, 36
- Tóth, G., Sokolov, I. V., & Gombosi, T. I. 2005, *JGRA*, 110, A12226
- Usmanov, A. V., Goldstein, M. L., Besser, B. P., & Fritzer, J. M. 2000, *JGR*, 105, 12675
- Usmanov, A. V., Matthaeus, W. H., Goldstein, M. L., & Chhiber, R. 2018, *ApJ*, 865, 25
- Valenti, J. A., & Fischer, D. A. 2005, *ApJS*, 159, 141
- van der Holst, B., Sokolov, I. V., Meng, X., et al. 2014, *ApJ*, 782, 81
- Verdini, A., & Velli, M. 2008, *ApJ*, 662, 669
- Vernazza, J. E., Avrett, E. H., & Loeser, R. 1981, *ApJ*, 45, 635
- Vidotto, A. 2021, *LRSP*, 18, 3

- Vidotto, A. A., Fares, R., Jardine, M., Moutou, C., & Donati, J.-F. 2015, [MNRAS](#), **449**, 4117
- Waite, I. A., Marsden, S. C., Carter, B. D., et al. 2017, [MNRAS](#), **465**, 2076
- Walker, G. A., Croll, B., Cuschnig, R., et al. 2007, [ApJ](#), **659**, 1611
- Wang, Y.-M., & Sheeley, N. R., Jr. 1992, [ApJ](#), **392**, 310
- Weber, L. J., & Davis, Jr. , 1967, [ApJ](#), **148**, 217
- Wedemeyer-Böhm, S. A., Lagg, A., & Nordlund, Å. 2009, [SSRv](#), **144**, 317
- Winter, L. M., & Balasubramaniam, K. S. 2014, [ApJL](#), **793**, L45
- Wood, B. E., Linsky, J. L., Ayres, T. R., et al. 1997, [ApJ](#), **478**, 745
- Wood, B. E., Müller, H.-R., Redfield, S., & Edelman, E. 2014, [ApJL](#), **781**, L33
- Wood, B. E., Müller, H.-R., Zank, G. P., et al. 2005, [ApJL](#), **628**, L143
- Yamashiki, Y. A., Maehara, H., Airapetian, V., et al. 2019, [ApJ](#), **881**, 114
- Young, P., Keenan, F. P., Milligan, R. O., & Peter, H. 2018, [ApJ](#), **857**, 5
- Yurchyshyn, V., Hu, Q., & Abramenko, V. 2005, [SpWea](#), **3**, S08C02